



UNIVERSITÀ
DEGLI STUDI
FIRENZE

FLORE

Repository istituzionale dell'Università degli Studi di Firenze

On salt marshes retreat: experiments and modeling toppling failures induced by wind waves

Questa è la Versione finale referata (Post print/Accepted manuscript) della seguente pubblicazione:

Original Citation:

On salt marshes retreat: experiments and modeling toppling failures induced by wind waves / M. Bondoni;S. Francalanci;L. Cappietti;L. Solari. - In: JOURNAL OF GEOPHYSICAL RESEARCH. - ISSN 0148-0227. - ELETTRONICO. - (2014), pp. 1-18. [10.1002/2013JF002967]

Availability:

This version is available at: 2158/842755 since: 2016-01-20T12:56:10Z

Published version:

DOI: 10.1002/2013JF002967

Terms of use:

Open Access

La pubblicazione è resa disponibile sotto le norme e i termini della licenza di deposito, secondo quanto stabilito dalla Policy per l'accesso aperto dell'Università degli Studi di Firenze (<https://www.sba.unifi.it/upload/policy-oa-2016-1.pdf>)

Publisher copyright claim:

(Article begins on next page)

RESEARCH ARTICLE

10.1002/2013JF002967

Key Points:

- We carried out laboratory experiments on wind waves impact on salt marsh edge
- We developed a model for the retreat of salt marshes due to toppling failures
- The theoretical model captures the observed salt marsh retreat

Correspondence to:

M. Bendoni,
mbendoni@dicea.unifi.it

Citation:

Bendoni, M., S. Francalanci, L. Cappiotti, and L. Solari (2014), On salt marshes retreat: Experiments and modeling toppling failures induced by wind waves, *J. Geophys. Res. Earth Surf.*, 119, doi:10.1002/2013JF002967.

Received 27 AUG 2013

Accepted 24 FEB 2014

Accepted article online 26 FEB 2014

On salt marshes retreat: Experiments and modeling toppling failures induced by wind waves

M. Bendoni¹, S. Francalanci², L. Cappiotti¹, and L. Solari¹

¹Department of Civil and Environmental Engineering, University of Florence, Firenze, Italy, ²CERAFRI—Center of Research and Advanced Education for Hydrogeological Risk Prevention, Retignano di Stazzema, Lu, Italy

Abstract Salt marshes are delicate ecosystems which are disappearing in many areas of the world, mainly due to increasing rates of sea level rise, subsidence, and anthropic pressure. The lateral erosion of the edge of salt marshes is one of the most important processes in determining changes in morphology, and wind waves have a key role in this retreat. Lateral retreat occurs by means of several types of mass failure processes, typically cantilever, sliding, and toppling. In the literature, no mechanistic models for the description of toppling failure are available. In this study, we performed a set of experiments to quantify the pressure field and the hydrodynamic forcing induced by wind waves during toppling failures of unstable blocks on a salt marsh edge. We propose a model interpreting toppling failure based on the experimental evidence as well as on the physics of the system. We model the system as a dynamic rigid block of cohesive soil, identified by the presence of a tension crack, subjected to hydrodynamic forces caused by impact of waves and resistive forces due to the block's weight and soil cohesion. The failure of the blocks occurs when the soil tensile strength is exceeded along the failure surface located at the base of the block. The model is able to reproduce failure processes observed in the laboratory. Moreover, the model reveals that the most critical conditions for marsh bank instability due to toppling failure are associated to the presence of water inside the tension crack and low water levels in front of the bank.

1. Introduction

Salt marshes are flat lands covered chiefly by halophytic vegetation periodically flooded by the sea due to tides [Allen, 2000], where fine sediments are transported by water and stabilized by vegetation [Boorman, 1995]. This natural system, together with meandering channel networks, is a part of tidal environments and lagoons whose evolution is controlled by complex and often nonlinear interactions including hydrodynamics, morphodynamics, and ecological processes. Salt marshes usually form in low-energy coastlines in temperate and high latitudes both in macrotidal and microtidal regimes [Allen and Pye, 1992]. Their characteristics change with latitude, and a broad range of salt marsh types can be identified based on vegetation, composition, and community structure [Adam, 1990].

Nowadays, increasing rates of sea level rise, subsidence, anthropic pressure, and the evident vanishing of large marsh areas all over the world, underline the importance of predicting the response of the tidal environment to environmental changes [van der Wal and Pye, 2004; Gedan et al., 2009; Kirwan and Temmerman, 2009]. For instance, in the case of the Venice Lagoon, salt marsh extension has more than halved in the last century [Cola et al., 2008]. Thus, in order to protect and promote an appropriate management of tidal environments, it is necessary to understand the relationships among the involved physical and biological processes (both natural and anthropic) and to develop modeling tools able to describe their evolution in short and long time scales. Van de Koppel et al. [2005] revealed the self organization properties of salt marsh ecosystems; Mariotti and Fagherazzi [2010] showed that retreat/progradation of a marsh scarp is the result of the interaction among vegetation, sediment supply, and sea level rise. Nevertheless, in both cases, wave erosion of marsh edge was rather simplified.

The erosion of the edge of the salt marshes is one of the most important processes in determining changes in morphology, and wind waves are directly involved in this retreat [Schwimmer, 2001; Moller and Spencer, 2002; Feagin et al., 2009; Marani et al., 2011; Moller, 2012]. The retreat of the marsh boundary is a complex phenomenon involving the characteristics of flow field, soil, vegetation, and bank geometry. We distinguish two fundamental ways in which the marsh scarp can retreat based on the size of the removed material:

surface erosion and mass failure. For our purposes, we use the terminology “surface erosion” to envisage the combination of both surface and mass erosions as described by *Winterwerp and van Kesteren* [2004] and *Winterwerp et al.* [2012]. In particular, by surface erosion, we consider the quasi-continuous detachment of particles and aggregate of particles (small lumps) from the surface whose size is considerably smaller with respect to the bank dimensions.

“Mass failure” is a discontinuous process of slump of whole portions of soil whose dimensions are comparable to the bank scale; it can happen in various ways such as rotational slips, cantilever failures, toppling, and other typologies of failures depending on the configuration of the bank itself. This latter process has been studied by various authors from a qualitative point of view or by conceptual models [*Allen*, 1989; *Pringle*, 1995; *Allen*, 2000; *Chauhan*, 2009].

In the literature, few attempts have been made to develop a mathematical description of the phenomenon, and usually, surface erosion and mass failures are gathered in an overall erosion rate formulation based on empirical data and field measurements [*Schwimmer*, 2001] as well as dimensional analysis [*Marani et al.*, 2011]. Analytical models are available to describe mass failures of the cantilever typology based on the stability of the geometrical profile of the bank [*van Eerd*, 1985; *Gabet*, 1998]. In this case, a block of sediment collapses from an undercut bank. On the other hand, toppling failures, for which the failure is triggered by a subvertical fracture, are not described analytically, except for rock mechanics [*Ashby*, 1971; *Goodman and Bray*, 1976; *Amini et al.*, 2009], even though different processes are involved. Importantly, field evidence shows that toppling failure can represent the most frequent mechanism of marsh edge deterioration in cohesive muddy systems [*Allen*, 1989], and this is triggered by the presence of tension cracks, in analogy with fluvial cases [*Thorne and Tovey*, 1981]. Tension cracks most frequently form at the end of the summer season due to the drying and shrinkage of the soil [*Allen*, 1989; *Morris et al.*, 1993]; furthermore, *Cola et al.* [2008] hypothesized that the formation of tension cracks induced by the cyclic oscillation of mean and effective stresses is due to tidal wave fluctuation. Recent experimental results [*Francalanci et al.*, 2013] have shown that toppling failure typology can occur during salt marsh retreat processes, especially under the effect of wind wave forcing, and can be triggered by the presence of tension cracks. Moreover, some toe scour at the bank edge tends to promote an overhanging bank profile, thus increasing instability.

In this research, we develop a theoretical model for toppling failure induced by wind waves. We carried out laboratory measurements of wave thrust and wave-induced pressure oscillation in the soil in a flume on physical models of a marsh bank, providing an estimation of the effect of waves impacting the bank. Experimental results are employed to characterize the hydrodynamic forces which are the input of the theoretical model. The application of the theoretical model to the experimental results shows the overall model capability of identifying the wave trains that can induce a toppling failure of the bank.

The rest of the paper is organized as follows: we first summarize the results of laboratory experiments devoted to the observations of the retreat of salt marsh edges [*Francalanci et al.*, 2013]; we then present new experiments aimed at characterizing the wave forcing effect on the marsh edge; then we propose a theoretical model interpreting the mechanism of failure due to the toppling of the soil blocks; finally, the theoretical model is tested against the experimental results.

2. Experimental Activity

The experiments presented in this work were built upon the work carried out by *Francalanci et al.* [2013] which focused on the retreat processes occurring on the marsh scarps induced by tide and wind wave hydrodynamic forcing and built the main framework for the identification and interpretation of different types of erosion mechanisms (Figure 1). First results from *Francalanci et al.* [2013] are summarized, then new experiments are presented.

2.1. Summary of the Experiments and Retreat Processes

The experiments were conducted in a glass wall wave current flume which was about 50 m long, 0.8 m wide, and 0.8 m deep. The wave current flume in front of the bank was narrowed to be 0.5 m wide for a length of about 8 m. This length was designed to allow the incoming waves to adapt to the narrowed width. Five resistive wave gauges were located along the wave current flume to measure the water level during the experiment with wave motion: two wave gauges were located close to the wave maker to measure the generated waves,

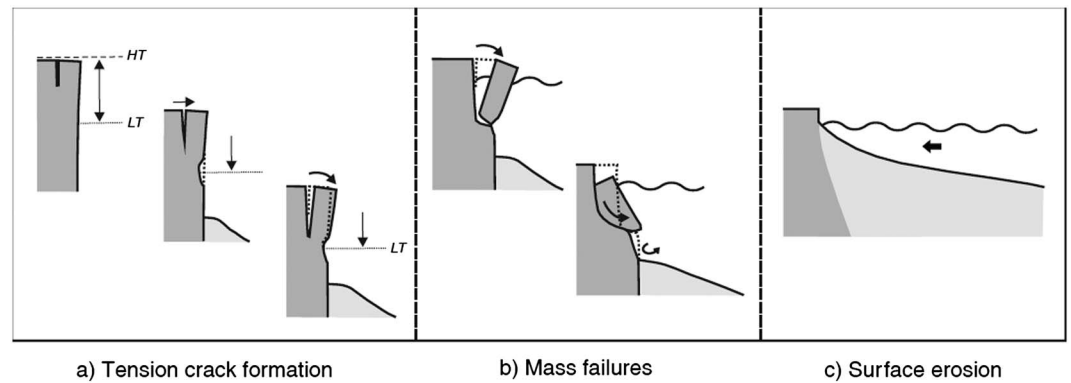


Figure 1. Typical mechanisms of failure observed in some of the experiments by *Francalanci et al.* [2013].

while three wave gauges were located in the narrowed channel close to the bank, spaced at 25 cm, to characterize the wave climate at the bank edge.

The physical models of the salt marsh were built at one end of the flume, while at the opposite end, irregular waves were generated by a hydraulic piston-type wave maker driven by a deterministic spectral amplitude method, according to *Hughes* [1995]. The reproduced salt marsh bank was 0.5 m wide, 0.6 m high, and about 1 m long. This bank height appears to be very similar to subvertical scarps of the marsh edges observed in several sites of the Venice Lagoon and in other marshes around the world.

Four series of experiments were carried out considering tidal waves and a combination of both tidal and wind waves as the hydrodynamic forcing and considering, for the same forcing, two identical banks with and without the inclusion of vegetation.

The following processes were observed and analyzed as a result of the experimental activity:

1. Under the effect of tidal wave oscillation, tension cracks developed on the top of the marsh scarp, both in the case of an unvegetated and a vegetated bank. The tension cracks became wider during a series of three tidal cycles reproduced in the experiments.
2. In experiments with both tidal and wind waves, the mass failure of large, unstable blocks on the marsh edge occurred during the first part of the experiment when the resistive forces were exceeded by destabilizing forces.
3. Tension cracks were presumed to trigger bank failure: waves induced a sort of “shaking” on a block identified by the presence of a tension crack. This process rapidly led to the failure of the block that overturned and slumped in front of the bank, i.e., by a toppling type of failure. In such cases, it may be the tensile strength rather than the shear strength of the soil which is exceeded. This hypothesis would lead to the identification of two different trigger mechanisms of failure, depending, indeed, on whether it is the tensile or the shear strength of the soil which is exceeded. Wave action may induce a torque on the failure surface leading to an alternating compression and traction of the soil fibers until the tensile strength threshold is reached.
4. Starting from an unstable configuration, the erosion rate decreased during the experiment. The mechanism of surface erosion (also called “particle-by-particle” erosion) was observed during the whole duration of the experiments, but is not discussed here, being beyond the scope of the present paper.
5. The effect of the presence of vegetation was to produce a delay in the mass failure of the vegetated clods, which was interpreted as having a strengthening effect on the bank.

The laboratory observations can lead to some qualitative interpretations of the failure mechanism. In a bank characterized by the presence of a tension crack, several forces act on the overhanging unstable block: block weight, hydrostatic water pressure due to the water in front of the block and possibly inside the crack, soil cohesion, and wave forcing. Their combination and the geometry of the block can lead to stable or unstable configurations and eventually to the failure of the block.

Note that both laboratory experiments and field observations gave evidence of a mechanism characterized by the rapid failure of the block on a bank with a developed tension crack (Figures 3a and 3b), together with the presence of overturned slumped blocks in front of the bank.

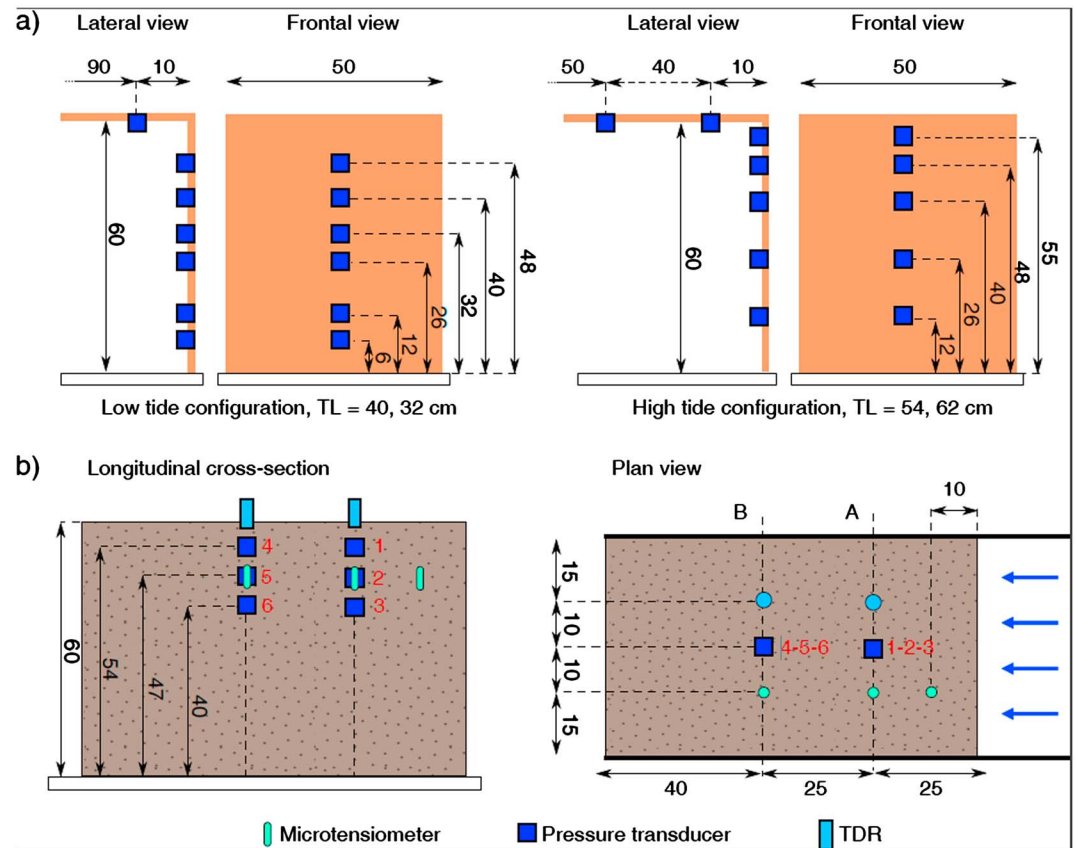


Figure 2. Experimental setup: (a) configuration of pressure transducers for measurements on a vertical wall, measurements are given in centimeter; (b) configuration of pressure transducers, pore water pressure, and water content sensors, measurements are given in centimeter.

Based on the previous observations, in section 3, we present a mathematical model describing the behavior of a block on the verge of collapse subjected to a time-dependent hydrodynamic forcing.

2.2. Experimental Setup

The experimental setup of the flume and the system of measurements for water levels are identical to *Francalanci et al.* [2013]. In addition, two different experiments were conducted to measure the pressure field in front of the marsh boundary and in the pore water.

The physical model for the first series of experiments was built with rigid impermeable material (plywood) since the soil in the reference environment has a low permeability (from 10^{-6} to 10^{-8} m/s). It was equipped with pressure transducers (PTs) as reported in Figure 2a, and it was aimed at evaluating the hydrodynamic force of the waves impacting on the marsh border at different water levels. The sampling rate of the PTs was set equal to 100 Hz with a measurement range between 0 and 1 kPa. We use these experiments to obtain a more detailed description of the wave forcing to be employed in the mathematical model described in section 3.

The second series of experiments investigated was devoted to study the propagation of the pressure wave within an erodible bank model while observing the erosion processes. The bank was built using the material collected in a salt marsh near Campalto, in the Venice Lagoon, consisting of fine sediment in the range of mud and clay (42% and 17%, respectively), with the remaining part in the range of very fine sand and including a small amount (around 5%) of organic matter. Following a procedure similar to that employed by *Nardi et al.* [2012] and by *Francalanci et al.* [2013], the bank model was progressively built by creating a series of 10 cm layers. A static load was applied to each layer for a minimum of about 24 h to allow for soil consolidation. The physical model of the salt marsh bank was equipped with the same PTs (Figure 2b) as the previous experiments and placed along the central axis of the bank to measure the wave-induced pressure in

Table 1. List of Laboratory Experiments (h is the Average Water Depth)^a

Experiment Series	Code	PTs-Tide Configuration	h (cm)
Pressure on a vertical wall (rigid model)	<i>Pwall32</i>	Low	32
	<i>Pwall40</i>	Low	40
	<i>Pwall54</i>	High	54
	<i>Pwall62</i>	High	62
Pressure inside the bank (erodible model)	<i>Pbank54</i>	Unique	54
	<i>Pbank62</i>	Unique	62
	<i>Pbank32</i>	Unique	32
	<i>Pbank40</i>	Unique	40
	<i>Pfail54</i>	Unique	54

^aThe experiments with the erodible model are listed in temporal order.

six positions inside the bank. Pore water pressures and water content inside the bank were measured by a series of microtensiometers and TDR (time domain reflectometry) sensors. Microtensiometers were located on a side of the bank edge to minimize their effects on bank erosion, while TDRs were positioned along the other side of the bank model.

For both series of experiments, the reference tidal wave was a simple semidiurnal tide with an approximated

period of 12 h. On the basis of the field observations, the tide excursion was set equal to 30 cm around the average water level in the flume imposed at an elevation of 47 cm above the bottom channel. In this way, the high tide level was set at 62 cm, that is, about 2 cm above the top of the reproduced bank which was therefore flooded. The low tide was set at 32 cm above the bottom channel.

We did not reproduce the tidal cycle as a continuous process, rather, we selected only different tidal levels in front of the salt marsh bank. The average level inside the wave current flume was changed by opening a valve or by pumping freshwater.

The wind waves were reproduced according to field data measured at a wavemeter station from the Venice Lagoon [see *Francalanci et al.*, 2013], which were analyzed in order to select the characteristic parameters of the wave spectrum. A target Joint North Sea Wave Project spectrum [*Hasselmann et al.*, 1973] was generated with a significant height of 10 cm, a significant period of 1.4 s, and a peak enhancement factor of $\gamma = 2$.

2.3. Experimental Activity and Procedure

A summary of all the experiments is reported in Table 1. For each series, the experimental protocol is described.

2.3.1. Pressure Field Distribution on a Vertical Marsh Edge (Rigid Model)

First, the pressure transducers were located along the middle vertical of a wooden rigid wall reproducing the marsh bank edge. Pressure measurements were collected in two different PT configurations, one for the high and one for the low tide. For each configuration, pressure measurements were carried out at two different average tidal levels corresponding to specific water depths h : 32 and 40 cm for the low tide and 54 and 62 cm for the high tide (Figure 2a).

After the transducers were installed, the water depth in the flume was adjusted to the simulated tidal level, and finally, the wind wave motion was started in the flume; each experiment lasted at least 5 min, which was a sufficient time to characterize the wave climate.

2.3.2. Pressure Field Inside the Bank (Erodible Model)

Pressure transducers were located inside the bank model during the construction of the physical model of the salt marsh. First, the water depth in the flume was adjusted to the imposed tidal level, then the wind wave motion was started in the flume and lasted about 5 min; during the experiment, videos and images were acquired. The following sequence of water depths was reproduced: 54 cm, 62 cm, 32 cm, and 40 cm. At the end of the experiment, the tension cracks that formed on the top of the marsh bank and the modified bank geometry were surveyed.

After the previous series of experiments, the water level was adjusted to 54 cm, and the experiment was started again (*Pfail54* in Table 1) to measure the pressure field during the failure process and to observe any main failure mechanisms. This experiment could be repeated only once, and it was divided into two slots which lasted 5 and 25 min, respectively.

3. Modeling of Toppling Failure

3.1. Formulation of the Problem

We propose here a simplified scheme for modeling retreat processes due to toppling failures: we consider a cross section of the bank in the x - z vertical plane which extends for a given width L , where an approximately

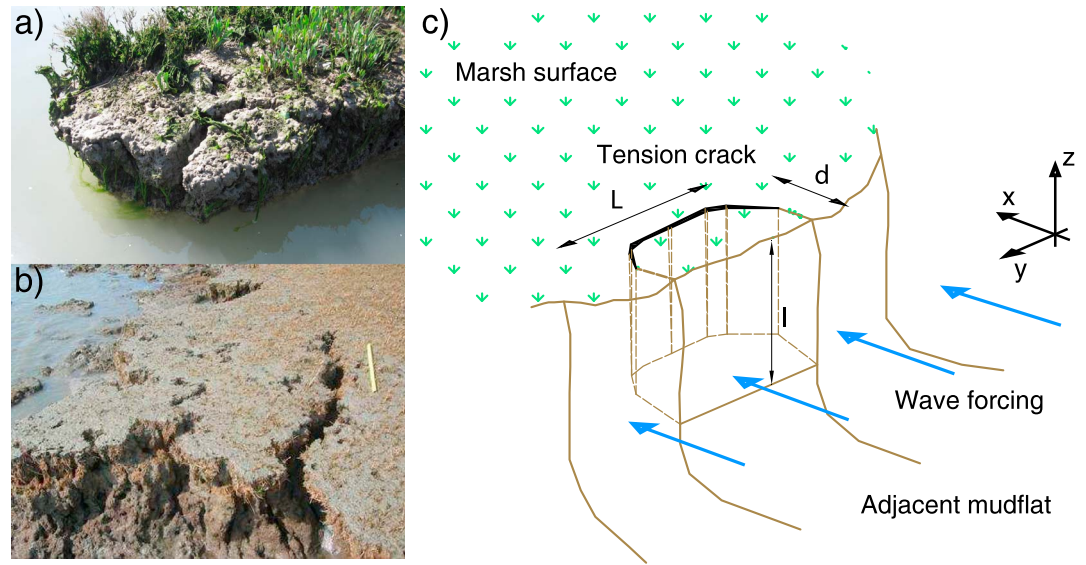


Figure 3. (a and b) Pictures of tension cracks on the surface of salt marshes (Figure 3b courtesy of G. Mariotti). (c) Sketch representing the unstable block due to the presence of a tension crack forced by waves. The thick black line identifies the geometry of the crack; dotted brown lines identify the hypothesized geometry of the block in the verge of failure.

prismatic block of cohesive soil is subjected to the action of the waves (Figure 3c). The block, modeled as a rigid body of mass m , is connected to the underlying layer by a system of spring and dashpot (i.e., a system to simulate the damping mechanism; the analytical treatment of the dynamic spring stiffness and damping coefficient can be found in the Appendix A) and identified by the presence of a tension crack (see the sketch in Figures 4a and 4b). The location, the depth of the crack, and the width of the block are deterministically characterized from experimental results and constitute a premise for the applicability of the model. The soil is considered homogeneous and isotropic and has a viscoelastic behavior, the dynamics of which are described by a Kelvin-Voigt model [Malkin and Isayev, 2006]. It is also impermeable with reference to the time scales involved in the process: representative values for the saturated water conductivity K_S ranges from 10^{-6} to 10^{-8} m/s for the soil of the salt marshes located in the lagoon of Venice [Cola et al., 2008].

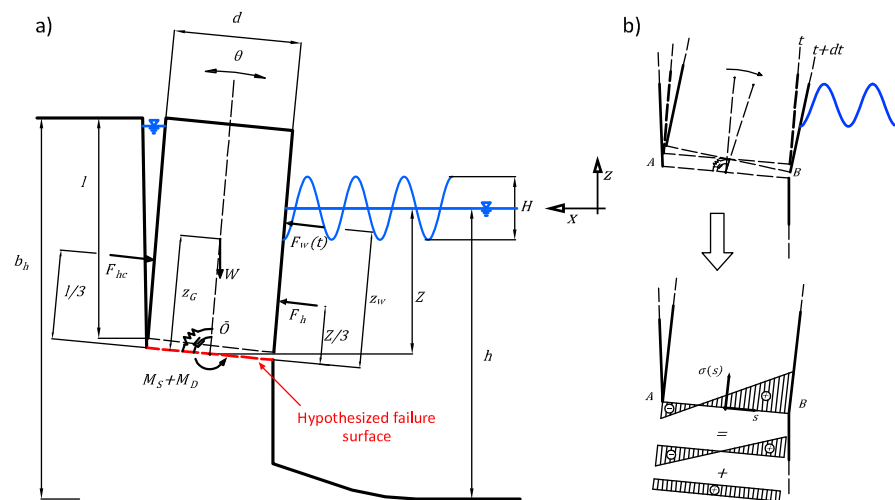


Figure 4. (a) Sketch of the cross section of the system upon which the dynamic model is based. The extension of the system in the orthogonal direction to x - z plane is determined by the width of the block L . (b) Schematic of the failure surface with the stress distribution induced by a small clockwise rotation of the block from its equilibrium configuration.

The block is subjected to several forces: gravity, hydrostatic thrust, and hydrodynamic thrust due to the impact of waves. It behaves like a dynamical system responding to external forcing with a small oscillation of an angle θ (positive clockwise) around an equilibrium configuration.

The assumptions and hypotheses made in order to simplify the studied system are discussed in the following paragraphs.

Forces acting laterally on side vertical surfaces of the block are neglected. This is also the case for the physical models of a salt marsh bank reproduced inside the wave flume, where the friction on the lateral wall, made of glass, can be neglected. This first assumption is also supported by model testing against experimental results.

Failure occurs once the tensile strength of the material is exceeded on at least one point of the failure surface, implicitly assuming that the fracture instantaneously propagates along the partialized failure surface. We hypothesize that the failure surface is plane and possibly tilted at a small angle θ_0 with respect to the horizontal. Its length and width are assumed equal to the block length d and width L (Figure 3c), and it is located at a depth from the marsh surface equal to the depth of the crack l (Figure 4a). Maximum tensile strength is assumed, at a first degree of approximation, as being equal to the soil cohesion measured through a consolidated undrained triaxial test. This varied from 5 to 20 kPa for the samples collected in the lagoon of Venice and was around 15.5 kPa for the sample collected in the wave flume [Francalanci *et al.*, 2013].

The initial equilibrium configuration in the absence of waves is characterized by an angle $\theta_0 + d\theta$ with respect to the vertical direction. The perturbation $d\theta$ represents a small clockwise rotation due to the moment induced by the weight of the block itself and is proportional to the inclination θ_0 . In presence of wave action, the block is partially free to oscillate due to the presence of soil at the back and the possible presence of water inside the crack. Thereby, counterclockwise rotation in respect to the initial configuration are not allowed (see Appendix A).

The failure surface does not change during the oscillation: the rotating point \bar{O} is located on the midpoint of the failure line and is fixed; so the neutral axis does not change its position with time during rotation. The reason for this assumption is to avoid having to implement, every time, an iterative procedure to locate the position of the neutral axis.

Block mass m_{block} is determined by height, length, width, and wet soil density, which are l , d , L , and ρ_s respectively. Water depth is identified by h , and Z represents the submergence of the rotating point \bar{O} with respect to the mean water level.

The moment and normal force due to the block weight, at an arbitrary time, are transmitted to the underlying layer resulting in the stress configuration qualitatively depicted in Figure 4b. A minus sign represents tension stresses, whereas a plus sign represents compression stresses.

3.2. The Model Equations

Toppling failure is assumed to occur when the rotation of the soil block gives rise to an excess of normal tensile stress. The governing equation for the rotation of the system can be written as

$$I \frac{d^2\theta}{dt^2} = \sum_i M_i \tag{1}$$

in which θ is the angle (positive clockwise) with respect to the equilibrium configuration, I is the moment of inertia of the block with respect to the point \bar{O} (including the contribution of the hydrodynamic mass), and M_i is the i th moment related to the point \bar{O} due to the forces acting on the block.

Following Oumeraci and Kortenhaus [1994], the hydrodynamic mass for rotational motions with respect to the base of the block can be estimated with

$$m_{\text{hyd,rot}} = 0.218 \rho_w LZ^2 \tag{2}$$

this term is included in the moment of inertia with respect to the point \bar{O}

$$I = m_{\text{block}} \left(\frac{l^2 + d^2}{12} \right) + (m_{\text{block}} + m_{\text{hyd,rot}}) \frac{l^2}{4} \tag{3}$$

with reference to Figure 4a, $M_s = -k_d\theta$ is the reaction moment of the spring, and $M_d = -c_d d\theta/dt$ is the reaction moment of the dashpot, respectively, modeling soil elasticity and viscosity. $W = \rho_s g \cdot dL$ is the block weight,

$F_h = \rho_w g L Z^2 / 2$ and $F_{hc} = \rho_w g L l^{*2} / 2$ are the hydrostatic thrust of water in front of the bank and inside the crack, and l^* represents the depth of the crack multiplied by the degree of filling of the crack due to the presence of water (for small oscillations of the angle theta, $\cos(\theta_0 + \theta) \approx 1$). The degree of filling is defined as the ratio between the water depth inside the crack and the depth of the crack itself. Parameter F_w is the hydrodynamic thrust due to water waves. Parameters k_d and c_d are, respectively, the dynamical spring stiffness and the damping coefficient, both depending on the frequency of the forcing. Parameters ρ_s and ρ_w are the density of soil and water; g is the acceleration of gravity. Based on the system of forces described above and assuming small rotations, $\sin(\theta_0 + \theta) \approx \theta_0 + \theta$, and substituting the moments in equation (1), we obtain

$$I \frac{d^2 \theta}{dt^2} + c_d \frac{d\theta}{dt} + k_d \theta = -F_h \frac{Z}{3} + F_{hc} \frac{l^*}{3} - F_w(t) Z_w(t) + W \frac{l}{2} (\theta_0 + \theta) \quad (4)$$

where the hydrodynamic thrust due to waves acts at a distance Z_w from the point \bar{O} . Since we consider small rotations, the direction of application of the forces can be considered parallel to the horizontal and independent from θ . This equation is converted to a system of two first order ordinary differential equations and then solved numerically using a fourth-order Runge-Kutta method with specific initial conditions for θ and $d\theta/dt$.

The stress acting on the failure surface is simply calculated assuming a linear stress-strain relation, strictly valid in the case of small deformations, and with the same behavior in compression and extension. The value of the total reaction moment M exerted on the failure surface is the sum of M_s and M_d , whereas the normal force exerted on it is $F_c = W \cos(\theta_0 + \theta) \cong W$. With these values, it is possible to calculate the stress acting on the failure surface. Considering a reference system centered in the point \bar{O} with s direction along the segment AB , positive from \bar{O} to B (Figure 4b)

$$\sigma(s) = \frac{M}{I_s} s + \frac{F_c}{dL} \quad (5)$$

where $I_s = d^3 L / 12$ is the moment of inertia orthogonal to the x - z plane of the failure surface. For the determination of σ , the neutral axis remains fixed during the time evolution of the system, and the failure criterion only regards the tensile strength of the material.

3.3. Determination of Wave Forcing

Wave thrust F_w is estimated through the classical Airy linear wave theory [Dean and Dalrymple, 1991] and the application of a correction factor determined from the present experimental measurements (see section 4.1). Knowing water depth h , water displacement η_i , and period T of a regular wave train moving toward an obstacle such as a vertical surface, it is possible to evaluate the wave thrust exerted on it. In the case that the forcing is characterized by an irregular wave series, the theoretical determination of the wave thrust is carried out applying linear wave theory to each wave defined when the surface elevation crosses the mean water level upward and continues until the next crossing point (the so-called zero-up crossing technique). The zero-crossing wave height is the difference in water surface elevation of the highest crest and lowest trough between successive zero crossings. Wave thrust is calculated without considering the effect of reflection.

The dynamic pressure is calculated from

$$p_d(z, t) = \rho_w g K_p(z) \eta_i(t) \quad (6)$$

where $K_p(z)$ is the pressure response factor accounting for the dynamic component due to water particle acceleration. Therefore, wave thrust can be calculated integrating hydrodynamic pressure from the bottom to the water-free surface and multiplying for the width of the block L . In the case of the wave crest overtopping the bank, the integration is extended up to the upper limit of the bank instead of the wave crest. The arm of the wave thrust with respect to the point \bar{O} is determined numerically from the following equation:

$$Z_w = Z + \frac{\int_{-Z}^{\eta(t)} z \cdot p_d(z, t) dz}{F_w(t)} \quad (7)$$

4. Experimental Results

In this section we report the results of the experimental activity aimed at quantifying the effect of wind waves on a vertical marsh edge both for the rigid and the erodible physical model.

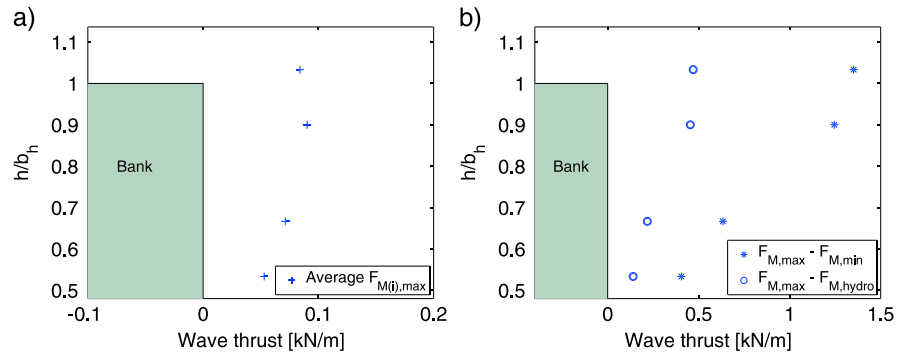


Figure 5. Wave thrust on vertical surface. (a) Average value of the maximum wave thrust of each wave at different values of water depth h (32 cm, 40 cm, 54 cm, and 62 cm) with respect to the bank height b_h . (b) Difference between maximum and minimum thrust (stars) and maximum and hydrostatic thrust (circles) measured during a single experiment at a specific water depth.

4.1. Estimate of the Wave Thrust on the Rigid Model

The measurement of the pressure field on a vertical wall provides an estimate of the hydrodynamic pressure on a vertical marsh edge, located orthogonal to the wave direction (Figure 2a). For each tidal level, we estimated the instant total thrust F_M exerted on the vertical edge by the wave motion. The F_M is calculated assuming the measurement of each PT representative of the pressure exerted on a portion of the wall. In Figure 5, the total thrust is reported for each of the four tidal levels; in particular, Figure 5a shows the average maximum thrust calculated by averaging the maximum thrust measured for each wave $F_{M(i),max}$; Figure 5b illustrates the difference between the absolute maximum $F_{M,max}$ and minimum thrusts $F_{M,min}$, and absolute maximum and hydrostatic thrusts $F_{M,hydro}$ measured during a whole experiment. We observed that the dynamic component of the thrust has a slower increase with increasing water level, gradually approaching the top of the bank. Indeed (see $h = 62$ cm for example) a fraction of the wave propagates over the bank, and it does not impact on the bank itself; this result is in agreement with Tonelli *et al.* [2010].

Results from wave thrust measurements and corresponding water displacement are used to better estimate the wave forcing for the model. In order to estimate a more accurate value for F_w , the value calculated through linear wave theory, F_T , is modified through a correction factor. To decouple the incident and reflected wave components, and thus to obtain the incident wave component in time domain, a modified version of Goda and Suzuki's [1976] method was used. Incident wave amplitude and phases were determined as a function of frequency, using the data collected by three wave gauges, considered in pairs. Then the incident time series was reconstructed as a sum of Fourier components.

From the time series of water levels representing the incident wave component, the value of F_T (theoretical wave thrust) was determined through classic linear theory integrating equation (6) on a vertical surface of the same frontal area of the physical model of the bank. A cross correlation analysis was then carried out between F_T and F_M to quantify the overlapping of the two time series, and the value of the normalized cross correlation reached a maximum value close to 0.9. Later, a zero-up crossing analysis was applied to both time series and the two series ΔF_T and ΔF_M , representing the magnitude of the wave thrust, were obtained. Each element corresponds to the difference between the maximum and minimum wave thrusts for a given wave. The above procedure was carried out for the data collected during the experiments *Pwall54* and *Pwall40*. In Figure 6, the scatterplot between ΔF_T and ΔF_M for the two experiments are reported, and it is possible to identify a linear relationship among the data. The linear regression line is constrained to pass through the origin, giving the following relations:

$$\Delta F_M = 1.66 \Delta F_T; \quad R^2 = 0.70; \quad h = 54 \text{ cm} \quad (8.a)$$

$$\Delta F_M = 1.80 \Delta F_T; \quad R^2 = 0.78; \quad h = 40 \text{ cm} \quad (8.b)$$

We set the correction factor applied to F_T to 1.75, which is a value closer to the result from the experiment at $h = 40$ cm during which no waves overtopped the bank, rather than the experiment at $h = 54$ cm which was characterized by the occurrence of some overtopping.

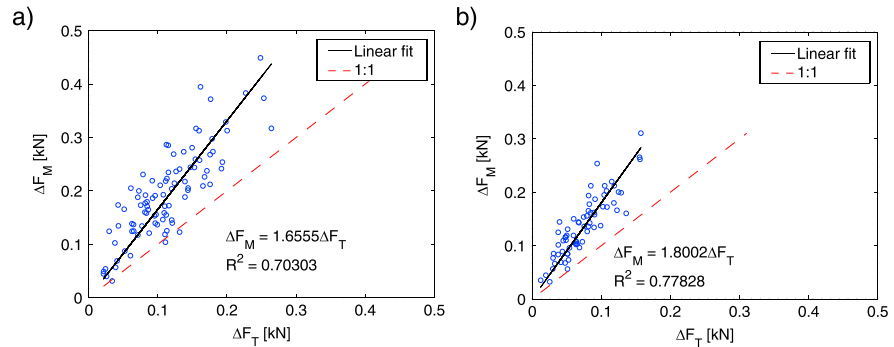


Figure 6. Scatterplot between ΔF_M and ΔF_T (blue circles) with linear fit curve (black line). (a) Experiment with mean water level at 54 cm; (b) experiment with mean water level at 40 cm.

In summary, to determine the time series as input data for the model, first, the incident wave component from measured water levels is calculated, then the wave thrust F_T is computed, and finally, the correction is applied to the result to obtain the forcing F_w and the moment arm Z_w to be used in equation (4).

4.2. Damping of Pressure Waves Inside the Erodible Model and Observed Failure Processes

For each pair of PTs located at the same depth (Figure 2b), we estimated the damping of the pressure waves while propagating in the porous soil, both with a spatial and temporal analysis.

First, a low-pass filtering procedure was carried out to remove the noise from the pressure measurement time series, then a zero-up crossing analysis of the values registered by pairs of PTs at the same depth was carried out, and the obtained amplitude of each pressure wave Δp associated to the PTs close to the marsh edge (PT numbers 1, 2, and 3) was compared to the damped pressure wave Δp_d of the farther PTs (numbers 4, 5, and 6), at the same depth. The results of Δp and Δp_d for $h = 54$ cm are reported in Figure 7: the damping of the pressure wave is higher for PTs 2 and 5 located 47 cm above the bottom channel, while it is smaller for PTs 3

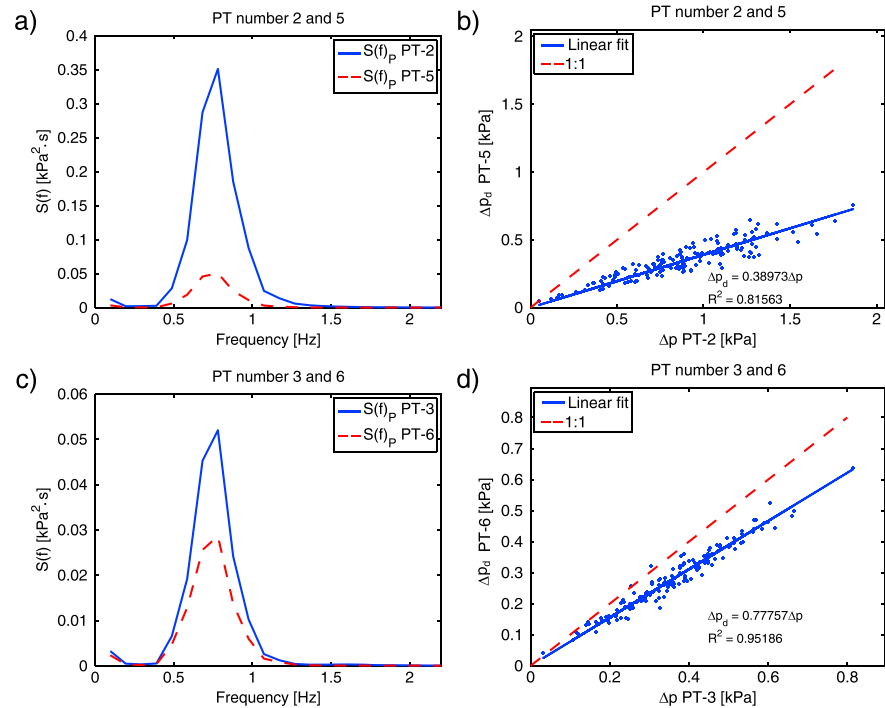


Figure 7. Damping of the pressure inside the bank during the experiment at mean water level at 54 cm. (a and c) Damping of the spectrum for a pair of PT located at the same depth. (b and d) Pressure fluctuation measured by a pair of PT located at the same depth. PTs 2 and 5 are located 13 cm below the bank surface, PTs 3 and 6 20 cm below bank surface.

Table 2. Dimensions of Collapsed Blocks Observed in the Experiments

Experiment Code	<i>d</i> (cm)	<i>l</i> (cm)	<i>L</i> (cm)
<i>U4.1HW</i> [Francalanci et al., 2013]	13	30	50
<i>Pfail54</i>	22	35	50
	15	30	50
	10	21	40

and 6 located at 40 cm; the regression line of the series and the line of perfect agreement are added in the plot. Results from the couple of PTs 1 and 4 located 54 cm above the bottom are not reported since PT 1 stopped functioning after 1 min after the beginning of the experiment.

The trend of the measured pressures is approximately linear and also in this case, the regression line is forced to pass through the origin. The other results, not shown here for brevity, showed consistent trends: for a tidal level of 40 cm, we observed a similar damping of pressure waves for the TP pair at height 47 and 40 cm.

Later, a spectral analysis with the Welch method [Welch, 1967] was performed for each pair of PTs, to estimate at which frequencies wave pressure amplitude is more reduced. The spectrum of each pair of PTs are drawn together and reported in Figure 7, for $h = 54$ cm. The energy spectrum is transported at frequencies lower than 1.5 Hz, and higher damping occurred close to peak frequency. The results from the spectral analysis are in agreement with the results of time domain analysis, indeed the damping of pressure waves appears to be much higher for the couple of PTs 2 and 5 located at 47 cm from the bottom of the channel with respect to the couple of PTs 3 and 6 located at 40 cm.

The failure processes observed during the experiments were similar to the mass failure processes described in Figure 1. We provide here a short description of the timing and the types of failure processes. During the experiment *Pbank54*, a toppling failure of the top block occurred in the first minute of the experiment: the soil was progressively stressed by the action of the waves, tension cracks appeared on the top of the bank, and finally collapse occurred. Approximately 2 min into the experiment, new cracks formed on the top of the bank in the interior marsh. Toppling of very small pieces from the edge occurred around 1'55" into the experiment, while at time 2'55" another failure of a small piece occurred on the front right side of the bank. The experiment *Pbank62* started from the final configuration of the previous one. Tension cracks on the top of the bank became wider, but no failures occurred during this experiment. The longitudinal profile of the bank and the position of the tension cracks were surveyed at the end of the *Pbank62* experiment.

During the experiments *Pbank40* and *Pbank32*, no mass failures occurred; tension cracks on the top of the bank became wider, and they were surveyed at the end of the *Pbank32* experiment.

In the *Pfail54* experiment, the pressure field was measured during the failure process. The starting configuration had very wide tension cracks, and an unstable block in the edge portion of the bank. At time 30" into the experiment, the tension crack measured several centimeters, then the block started to oscillate (time 45"), and finally, it failed (around time 55"). At time 1'10", we observed a second toppling failure, more rapid than the first one. The third toppling occurred immediately after the second, on the right side of the bank. The experiment was characterized by the occurrence of wave overtopping and then the cracks were filled with water. This configuration led to imbalanced forces at wave trough. At this stage, the water inside the crack could push the block toward the channel without encountering any resistance from soil or fluid. This was identified as one of the most significant processes leading to the failure of a block. The above described toppling failures will be used in the next section for the testing of the proposed model.

Approximately 3' into the experiment *Pfail54*, a high turbulence zone was observed in the upper part of the bank due to the energy of the impacting waves. Small pieces and single particles were frequently removed during this part of the experiment. This process of intense surface erosion lasted several minutes, then the exterior PT was removed. In Table 2, the dimensions of the collapsed blocks used in the simulations are reported; videos of these failures were selected as additional materials for a better description of the observed processes, available online as "supporting information".

5. Test of the Model

Four toppling failures were chosen to test the model's ability to identify the incipient failure of an unstable block. These blocks were roughly prismatic and large enough to be well described by the model. Simulations of toppling failure were carried out for four events; one observed after around 30 s from the beginning of the experiment identified by the code *U4.1HW* [Francalanci et al., 2013] and the remaining three pertaining to experiment *Pfail54*.

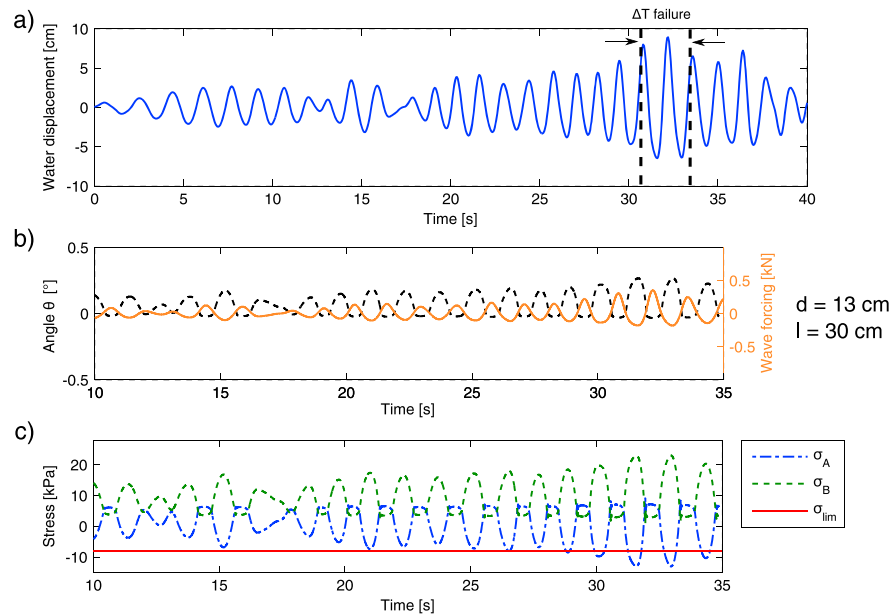


Figure 8. Results from the model test on the experiment named *U4.1HW* [Francalanci et al., 2013] with block height and length, respectively, 30 cm and 11 cm. (a) Water displacement and time interval at which the failure occurs (blue continuous line). (b) Time evolution of the angle θ (black dashed line) and of the wave hydrodynamic forcing (orange line). (c) Time evolution of the stress at the inner point (blue dash-dotted line) and at the outer point of the failure surface (green dashed line) and limit tensile strength (red line).

The results are plotted in Figures 8 and 9. Table 3 lists the values of the empirical and theoretical parameters used in the simulations. The value of cohesion, representing the tensile strength, the value of soil wet density, and the value of void ratio chosen to calculate the shear modulus through equations (A5) and (A6) are taken from the results of the geotechnical analysis of a sample collected in the field [see Francalanci et al., 2013]. This is because the laboratory analysis of the sample collected at the end of experiment *U4.1HW* experienced a very high water content, resulting in an unrepresentative value of the void ratio and soil wet density.

Figure 8a and 9a show the time series of water displacement corresponding to incident waves. For each failure, we recorded the time and duration of failure. Figures 8b and 8c and 9b–9g show the time evolution of the most significant variables of the model: the wave hydrodynamic forcing on the unstable block and the response of the angle θ with respect to time and the time evolution of the stress at two extreme points of the failure surface. The failure is predicted to occur when the tensile strength is exceeded in at least one point of the failure surface. It is possible to observe how the model is able to capture, in all but the first failure of *Pfail54*, the wave train leading to block failure. In the case of the first failure, the value of d (22 cm) is higher than for the other blocks, and this shortcoming of the model could be explained by the need to introduce a progressive failure mechanism (see section 7). For the second and third failures of experiment *Pfail54*, the wave groups responsible for failure are identified by the model, and in the case of the third failure, several waves brought the stress significantly close to the limit assumed for the tensile strength before the failure occurs. The failure of experiment *U4.1HW* occurred around 30 s into the experiment. The wave group responsible for the failure is clearly recognizable, and the maximum tensile stress exerted on the point A of the failure surface is reached at wave trough.

6. Discussion

The discussion is focused on various aspects and limitations of the proposed toppling model: (i) the role of water inside the tension crack during the failure process and the dynamic response of the system, (ii) the least stable condition for block stability, (iii) tension crack formation, (iv) effect of vegetation on toppling failure, and (v) the deterministic nature of many parameters and of input data for the model.

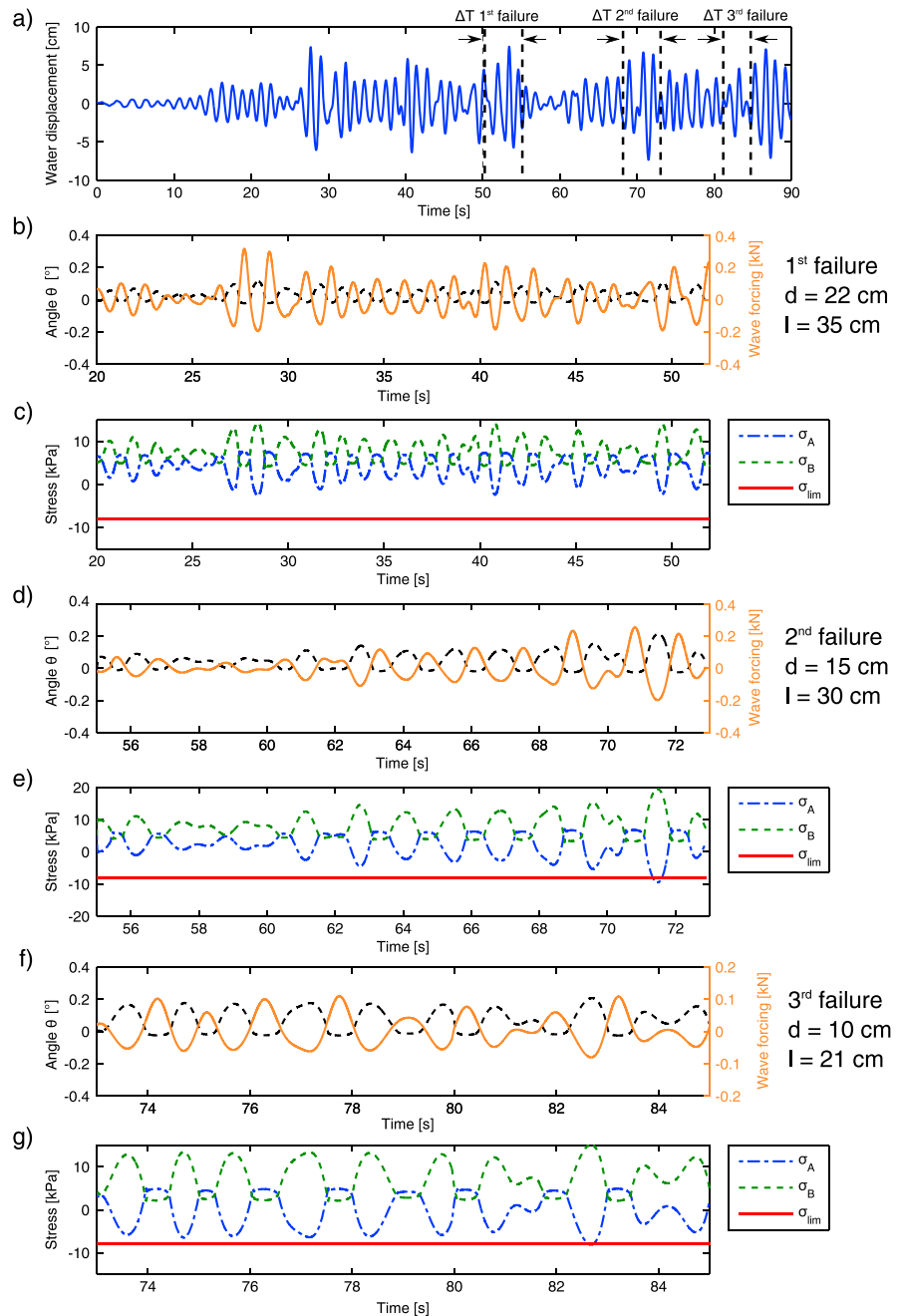


Figure 9. Results from the model test on the experiment *Pfail54*. (a) Water displacement (blue continuous line) and time interval in which failure occurred (black dashed lines). (b, d, and f) Time evolution of the angle theta (black dashed line) and of the wave hydrodynamic forcing (orange line). (c, e, and g) Time evolution of the stress at the inner point (blue dash-dotted line) and at the outer point of the failure surface (green dashed line) and limit tensile strength (red line). Each pair of pictures corresponds to a specific failure event.

Regarding the first point, the laboratory observations revealed that toppling failures are triggered by the presence of tension cracks. In all observed cases, at the failure, the crack was filled with water due to the wave overtopping of the marsh bank, and we argue that the presence of water inside the crack is crucial in promoting the failure of an unstable block. In the framework of the model, the failure can only occur when there is an imbalance between the forces acting on the block, leading to an excess of tensile stress on the failure surface. This condition happens more frequently at wave trough when the crack is filled with water. In such a case, the block can be pushed enough toward the channel to reach the tensile stress

Table 3. Values for the Empirical and Theoretical Parameters in the Present Simulations

Empirical Parameter	Value
Bank height	60 cm
ρ_s wet soil density	1700 kg/m ³
e_0 void ratio	1.296
c' cohesion	8 kPa
h water depth	54 cm
Theoretical Parameter	Value
θ_0	0°
ν Poisson's coefficient	0.5
Degree of filling of the crack	0.9
C_θ tuned by authors, see equation (A3)	5×10^3

limit. At wave crest, when the maximum thrust on the bank is exerted, the block is constrained to not oscillate counterclockwise due to the presence of water and of the stable bank behind it. The constraint to oscillation is included in the model by increasing the spring stiffness when the angle θ reaches negative values. Physically it means that the block can rotate counterclockwise until it roughly reaches its initial configuration. At this point, the further small counterclockwise rotation induced by the wave provides elastic potential to the system that is subsequently released at wave trough

when the block is free to rotate clockwise. This dynamic effect seems to be significant in the maximum tensile stress exerted on the failure surface.

To test these mechanisms, the model was run for a generic geometric configuration (bank height = 80 cm, $d = 25$ cm, $l = 45$ cm, and $h = 70$ cm), considering the cases of crack filled or not filled with water. Results were obtained for the same regular wave forcing with $H = 14$ cm and $T = 1.5$ s (Figure 10). Furthermore, to point out the dynamic character of the response of the system, we run a simulation using a simplified static approach in which we evaluate the synchronous response of the system to a fixed water level set equal to the lowest value reached at wave trough during the corresponding dynamic case. The stress related to this latter static case acting on the point A, $\sigma_{A,s}$, is reported in Figure 10. It is possible to observe that the stress reaches higher values when the crack is filled with water, and point A is subjected alternately to positive and negative stress whereas point B is always compressed. In the case where the crack was not filled with water, both points A and B were compressed for the most part of the simulation due to the weight of the block itself. Negative stresses (traction) at point A are reached at the wave trough, and they are significantly smaller (in absolute value) with respect to the negative stresses reached during the simulation with the filled crack.

Note that in both cases, the dynamic response of the system deeply affects the stress distribution on the failure surface. A much simpler calculation based on a purely static response of the system to a given water level would lead to rather different results. It therefore appears that a dynamic modelling of the system is necessary to predict the block failure.

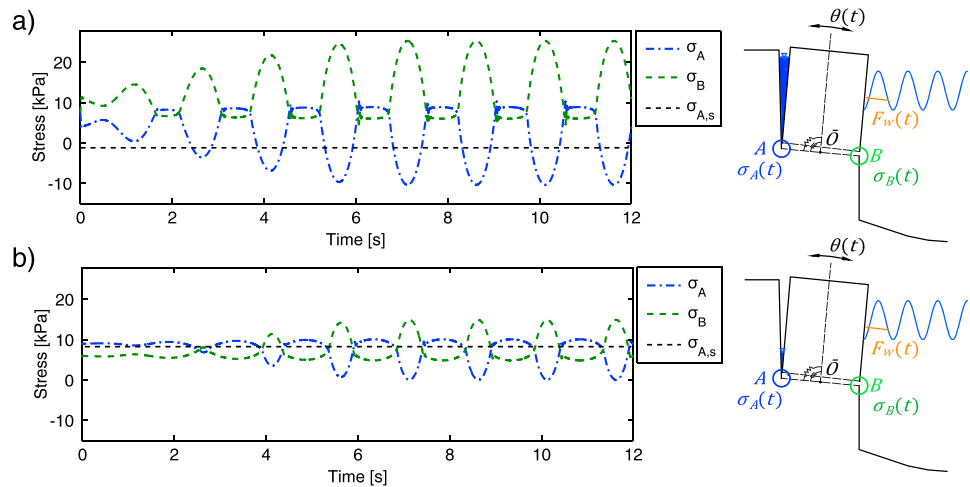


Figure 10. Comparison between the behavior of the model in the case when the crack is (a) filled or (b) not filled with water. The blue dash-dotted line represents the time evolution of the stress at the bottom of the tension crack in the inner point of the failure surface. The green dashed line represents the stress at the external point of the failure surface.

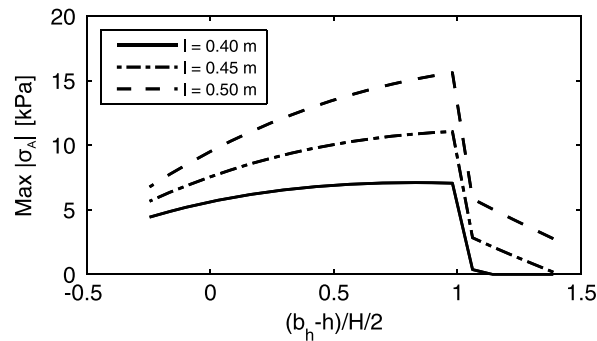


Figure 11. Maximum tensile stress exerted on the failure surface with the change of the parameter P determining the varying water depth h in front of the bank. Simulations are carried out with $H_i = 0.14$ m, $\chi = 0.75$, $T = 1.5$ s, $b_h = 0.8$ m, $d = 0.2$ m, and $L = 0.5$. The continuous line corresponds to $l = 0.40$ m, the dash-dotted line $l = 0.45$ m, and the dashed line to $l = 0.50$ m.

the instability at the wave trough. However, this condition occurs when the waves are high enough to overtop the bank. Therefore, it is useful to use the relative bank freeboard

$$P = \frac{b_h - h}{H/2} \quad (9)$$

where b_h is the bank height, and H is the wave height at the bank edge assuming a reflection coefficient χ of 0.75. The maximum values of tensile stress exerted on the failure surface for different simulations varying the parameter P (at the variation of h) are reported in Figure 11 (incident wave height $H_i = 0.14$ m, $T = 1.5$ s, $b_h = 0.8$ m, $d = 0.2$ m, $L = 0.5$, and $l = 0.40$ for the continuous line, $l = 0.45$ m for the dash-dotted line and $l = 0.50$ m for the dashed line). It is possible to observe that higher values of tensile stress are reached when P is close to 1, while they decrease rapidly when P increases above 1. For negative values of P , when the bank is completely flooded, the stress continues to decrease, and such configuration becomes less critical for bank stability. Hence, for a specific bank and wave height, the most critical condition for bank stability will be when P is a little smaller than 1, which means that the water depth is the minimum value that allows the filling of the crack by wave overtopping.

Regarding (iii), since the presence of cracks is crucial in promoting bank retreat, their formation deserves more attention. Some authors proposed different mechanisms for their occurrence in marsh environment: desiccation processes across seasonal variation [Allen, 1989; Morris *et al.*, 1993] and cyclic oscillation of mean and effective stresses due to tide [Cola *et al.*, 2008]. Both mechanisms act at large time scale, and they involve filtration processes. The formation of tension crack is presumably related to the soil characteristics and to bank edge geometry, leading to the hypothesis that a typical distance of tension crack from the marsh edge exists. Nevertheless, during the experimental activity, we observed the formation of vertical cracks both during the tidal experiments and during wave action. In particular, crack formation is a crucial step which announces the successive mass failure, and cracks continuously form while the bank is retreating. In fact, wave dynamic loading seems able to weaken a portion of the bank leading to the formation of a crack, similar to the process proposed by Adams *et al.* [2005] for rocky cliffs in coastal areas. This mechanism acts at a shorter temporal scale, and it does not directly involve filtration processes since muddy banks have generally low-permeability coefficients. For this reason, the investigation on this aspect might start from the approach proposed by Adams *et al.* [2005] adapted to cohesive banks.

Future developments will also include detailed field surveys of position and geometry of the cracks and distance from bank edge.

Regarding (iv), the role played by vegetation in the failure processes is still an open issue. On one hand, vegetation can presumably increase filtration velocity and porosity of the soil, on the other hand, the root mat can create additional cohesion, thus reducing the depth of the crack and delaying the failures of the vegetated blocks. When included in the toppling model, the effect of vegetation may produce a delay of the mass failure, but a more detailed description of the root mat structure and of the soil stress characteristic would be needed. In particular, in the model, failure is considered to occur instantaneously once a specific threshold of

stress is exceeded, while the inclusion of the vegetation requires the progressive failure, accounting for gradual detachment of the block from the failure surface due to the repeated and cumulated forcing of waves.

Regarding the last issue, the model represents a first attempt to describe the physics behind the toppling failure for cohesive banks. Having this in mind, many parameters have been assigned from experimental investigations or from theoretical analysis, and they are deterministically assumed as input data during simulations. Some of these parameters require a deeper investigation: the values of void ratio, shear modulus, wet soil density, and cohesion can be affected by uncertainties from laboratory analysis and sample collection. Furthermore, the location, the depth of the crack, and the width of the block chosen for the simulations were measured with a certain degree of approximation due to the presence of water in the channel and due to a degree of irregularity in the geometry of the blocks.

7. Conclusions

The present work focuses on salt marsh retreat processes, due to toppling, induced by wind waves. We developed a theoretical model for identifying the stability of soil blocks oscillating under the impact of waves. Moreover, we carried out flume experiments to measure the hydrodynamic forces acting on a salt marsh edge and the transmission of the pressure wave inside the soil.

Laboratory observations show that toppling failures are triggered by the presence of tension cracks and that block geometries have a certain degree of variability. The experimental data were crucial in determining many empirical parameters used as input data for the model, and they also constituted the test cases for the toppling failures of unstable blocks under given hydrodynamic forcing.

The model provides a wave by wave description of the hydrodynamic forcing rather than averaging over longer time intervals, since mass failure is modeled as a discontinuous process. The testing of the model against experimental data showed that the model is able to predict the toppling failure and the group of waves which produced the final detachment of the unstable blocks in three of the four recorded cases.

Finally, the simulations have demonstrated that the conditions of (i) water inside the tension crack and (ii) low water levels in front of the bank are the most unfavorable for promoting bank instability. Importantly, the dynamic response of the system appears to be crucial in predicting bank instability, as several factors, such as elastic potential energy accumulated by the system during compression and released during the wave draw down, and inertial effects, lead to higher stresses. A simple static model based on a synchronous response of the system to a given water level would lead to smaller stresses and a more stable condition.

Hence, the model constitutes a first tool for predicting the stability of cohesive banks which are experiencing erosion induced by wind waves, useful in management and protection of salt marsh areas.

Future developments of the present model will cover several aspects, i.e., the inclusion of vegetation on bank stability, the triggering mechanism for tension crack formation, and the 3-D character of the geometry of the unstable soil blocks, including the effect of lateral resisting forces.

Appendix A: Determination of Dynamic Spring Stiffness k_d and Damping Coefficient c_d

To solve equation (4), it is necessary to calculate the values of the dynamic spring stiffness and the damping coefficient, $k_d(\omega)$ and $c_d(\omega)$, where $\omega = 2\pi/T$ is the wave frequency. In order to do so, we refer to the principles of soil dynamics and soil foundation interaction. In the model, it is assumed that the failure surface between the failing block and the underlying soil behaves similarly to the contact surface between soil and foundation.

Parameters k_d and c_d take different values based on the frequency of the forcing and on the vibration mechanism [Gazetas, 1990]. In particular, the two coefficients are composed of a static and a dynamic contribution. The former depends on the characteristics of the soil and the geometrical dimensions of the interaction surface between the soil and the foundation (in the present model, it corresponds to the failure surface maintaining the block attached to the underlying layer). The latter also depends on the principal frequency of the forcing term. To determine such values, it is necessary to obtain the static values k_s and c_s and then to apply a correction to take into account their variation due to the external forcing.

The static value k_s of the spring stiffness for a rectangular surface (dimensions L and d with $L > d$) and the rocking vibration mode around the major axis, can be calculated as follows:

$$k_s = \frac{G}{1-\nu} I_s^{0.75} \left(\frac{L}{d}\right)^{0.25} \left(2.4 + 0.5 \frac{d}{L}\right) \quad (\text{A1})$$

where G is the shear modulus of the soil and ν is the Poisson's ratio.

The correction $K(\omega)$ for the dynamic stiffness coefficient is determined through the following relation:

$$K(\omega) \cong 1 - 0.2a_0 \quad (\text{A2})$$

where $a_0 = \omega \cdot d / (2V_s)$ and V_s is the shear wave velocity. Then $k_d(\omega) = k_s \cdot K(\omega)$.

The authors impose a modification of the dynamic stiffness coefficient to constraint oscillation. Indeed the rotation of the block toward the stable marsh is inhibited by the presence of water and of soil over the crack. It is assumed that when the angle θ assumes negative values (the block tends to rotate counterclockwise), k_d increases exponentially, proportional to θ according to the following equation:

$$k'_d = k_d \exp(-C_\theta \cdot \theta) \quad (\text{A3})$$

where C_θ is a constant to be chosen large enough not to allow significant counterclockwise rotation ($C_\theta = 5 \cdot 10^3$).

The value of damping coefficient, c_d , is calculated from the expression

$$c_d = \rho_s V_{La} I_s \cdot C(\omega) \quad (\text{A4})$$

where ρ_s is the soil wet density, V_{La} is the "Lysmer's analog" wave velocity, and $C(\omega)$ is the correction coefficient depending on L/d and a_0 from Gazetas [1990].

For cohesive normally consolidated soils with $\nu=0.5$ (undrained load condition in sature soil), G can be evaluated through the void ratio e_0 , the parameter A (ranging from 200 to 400) and the confining pressure σ'_0 [Marcuson and Wahls, 1972]

$$G = A \cdot f(e_0) \cdot \sigma'_0 \quad (\text{A5})$$

in which

$$f(e_0) = \frac{(2.97 - e_0)^2}{1 + e_0} \quad (\text{A6})$$

and

$$\sigma'_0 = \rho_s g l \quad (\text{A7})$$

Acknowledgments

Simonetta Cola is acknowledged for her valuable comments and Stefano Renzi for his advice at the beginning of the work. The experiments were carried out founded by the Italian Ministry of University and of Scientific and Technological Research in the framework of the National Project "Ecomorphodynamics of tidal environments and climate change" (PRIN 2008), cofounded by the University of Florence. The second author received financial support in the framework of the Project "MITI-Innovative Methodologies for the Protection of Drainage Basin and Coastal Areas," founded by Tuscany Region. The Editor, the Associate Editor Simon Mudd and two anonymous referees are acknowledged for providing useful comments and improving the presentation of this work.

References

- Adam, P. (1990), *Saltmarsh Ecology*, 461 pp., Cambridge Univ. Press, Cambridge.
- Adams, P. N., C. D. Storlazzi, and R. S. Anderson (2005), Nearshore wave-induced cyclical flexing of sea cliffs, *J. Geophys. Res.*, *110*, F02002, doi:10.1029/2004JF000217.
- Allen, J. R. L. (1989), Evolution of salt marsh cliffs in muddy and sandy systems: A qualitative comparison of British west-coast estuaries, *Earth Surf. Processes Landforms*, *14*, 85–92.
- Allen, J. R. L. (2000), Morphodynamics of Holocene salt marshes: A review sketch for the Atlantic and southern North Sea coasts of Europe, *Quat. Sci. Rev.*, *19*(12), 1155–1231, doi:10.1016/S0277-3791(99)00034-7.
- Allen, J. R. L., and K. Pye (1992), Coastal saltmarshes: Their nature and importance, in *Saltmarshes: Morphodynamics, Conservation and Engineering Significance*, edited by J. R. L. Allen and K. Pye, pp. 1–18, Cambridge Univ. Press, Cambridge, U. K.
- Amini, M., A. Majdi, and Ö. Aydan (2009), Stability analysis and the stabilization of flexural toppling failure, *Rock Mech. Rock Eng.*, *42*, 751–782, doi:10.1007/s00603-008-0020-2.
- Ashby, J. (1971), Sliding and toppling modes of failure in models and jointed rock slopes, MS thesis, Imperial College, University of London, London, U. K.
- Boorman, L. A. (1995), Sea level rise and the future of the British coast, *Coastal Zone Topics Processes Ecol. Manage.*, *1*, 10–13.
- Chauhan, P. S. (2009), Autocyclic erosion in tidal marshes, *Geomorphology*, *110*, 45–57, doi:10.1016/j.geomorph.2009.03.016.
- Cola, S., L. Sanavia, P. Simonini, and B. Schrefler (2008), Coupled thermohydrromechanical analysis of Venice lagoon salt marshes, *Water Resour. Res.*, *44*, W00C05, doi:10.1029/2007WR006570.
- Dean, R. G., and R. A. Darlymple (1991), *Water Wave Mechanics for Engineers and Scientists*, Adv. Ser. Ocean Eng., vol. 2, 368 pp., World Sci., Singapore.
- Feagin, R., S. Lozada-Bernard, T. Ravens, I. Moller, K. Yeager, and A. Baird (2009), Does vegetation prevent wave erosion of salt marsh edges?, *Proc. Natl. Acad. Sci. U.S.A.*, *106*(25), 10,109–10,113, doi:10.1146/annurev.earth.35.031306.140128.

- Francalanci, S., M. Bondoni, M. Rinaldi, and L. Solari (2013), Ecomorphodynamic evolution of salt marshes: Experimental observations of bank retreat processes, *Geomorphology*, *195*, 53–65, doi:10.1016/j.geomorph.2013.04.026.
- Gabet, E. J. (1998), Lateral migration and bank erosion in a saltmarsh tidal channel in San Francisco bay, California, *Estuaries*, *21*(4B), 745–753.
- Gazetas, G. (1990), Cap. 15 Foundation Vibrations, in *Foundation Engineering Handbook*, edited by H. Y. Fang, pp. 553–593, Kluwer Academic Publishers, Massachusetts, U.S.A.
- Gedan, K., B. Silliman, and M. Bertness (2009), Centuries of human-driven change in salt marsh ecosystems, *Annu. Rev. Mar. Sci.*, *1*, 117–141.
- Goda, Y., and Y. Suzuki (1976), Estimation of incident and reflected waves in random wave experiments, in *Proc. 15th Int. Conf. Coastal Eng.*, pp. 828–845, ASCE, Hawaii.
- Goodman, R. E., and J. W. Bray (1976), Toppling of rock slopes, *ASCE Specialty Conf. Rock Eng. Found. Slopes*, *2*, 201–234.
- Hasselmann, K., et al. (1973), Measurements of wind-wave growth and swell decay during the Joint North Sea Wave Project (JONSWAP), *Erganzungsheft zur Deutschen Hydrographischen Zeitschrift Reihe A*, *8*, 95.
- Hughes, S. A. (1995), *Physical Models and Laboratory Techniques in Coastal Engineering*, Adv. Ser. Ocean Eng., vol. 7, 560 pp., World Sci., Singapore.
- Kirwan, M. L., and S. Temmerman (2009), Coastal marsh response to historical and future sea-level acceleration, *Quat. Sci. Rev.*, *28*, 1801–1808, doi:10.1016/j.quascirev.2009.02.022.
- Malkin, A. Y., and A. I. Isayev (2006), *Rheolog. Concepts, Methods and Applications*, ChemTech, Toronto.
- Marani, M., A. D'Alpaos, S. Lanzoni, and M. Santalucia (2011), Understanding and predicting wave erosion of marsh edges, *Geophys. Res. Lett.*, *38*, L21401, doi:10.1029/2011GL048995.
- Marcuson, W. F., III, and H. E. Wahls (1972), Time effects on the dynamic shear modulus of clays, *J. Soil Mech. Found. Div., ASCE*, *98*(12), 1359–1373.
- Mariotti, G., and S. Fagherazzi (2010), A numerical model for the coupled long-term evolution of salt marshes and tidal flats, *J. Geophys. Res.*, *115*, F01004, doi:10.1029/2009JF001326.
- Moller, I. (2012), Bio-physical linkages in coastal wetlands – Implications for coastal protection, paper presented at, in *NCK-Days 2012, Crossing Borders in Coastal Research: Jubilee Conference Proceedings*, edited by W. M. Kranenburg, E. M. Horstman, and K. M. Wijnberg, pp. 51–60, University of Twente, The Netherlands.
- Moller, I., and T. Spencer (2002), Wave dissipation over macro-tidal saltmarshes: Effects of marsh edge typology and vegetation change, *J. Coastal Res.*, *S136*, 506–521.
- Morris, P. H., J. Graham, and D. J. Williams (1993), Cracking in drying soils, *Int. J. Rock Mech. Mining Sci. Geomech. Abstr.*, *30*(2), 263–277.
- Nardi, L., M. Rinaldi, and L. Solari (2012), An experimental investigation on mass failures occurring in a riverbank composed of sandy gravel, *Geomorphology*, *163–164*, 56–69, doi:10.1016/j.geomorph.2011.08.006.
- Oumeraci, H., and A. Kortenhaus (1994), Analysis of the dynamic response of caissons breakwaters, *Coastal Eng.*, *22*, 159–183.
- Pringle, A. W. (1995), Erosion of a cyclic saltmarsh in Morecambe Bay, north-west England, *Earth Surf. Processes Landforms*, *20*, 387–405.
- Schwimmer, R. (2001), Rates and processes of marsh shoreline erosion in Rehoboth Bay, Delaware, U.S.A., *J. Coastal Res.*, *17*(3), 672–683, doi:10.1016/j.csr.2009.08.018.
- Thorne, C. R., and N. K. Tovey (1981), Stability of composite river banks, *Earth Surf. Processes Landforms*, *20*, 469–484.
- Tonelli, M., S. Fagherazzi, and M. Petti (2010), Modeling wave impact on salt marsh boundaries, *J. Geophys. Res.*, *115*, C09028, doi:10.1029/2009JC006026.
- van Eerd, M. M. (1985), Salt marsh cliff stability in the Oosterschelde, *Earth Surf. Processes Landforms*, *10*, 95–106.
- van de Koppel, J., D. van der Wal, J. Bakker, and P. Herman (2005), Self-organization and vegetation collapse in salt marsh ecosystems, *Am. Nat.*, *165*, E1–E12.
- van der Wal, D., and K. Pye (2004), Patterns, rates and possible causes of saltmarsh erosion in the Greater Thames area (UK), *Geomorphology*, *61*, 373–391, doi:10.1016/j.geomorph.2004.02.005.
- Welch, P. D. (1967), The use of Fast Fourier Transform for the Estimation of Power Spectra: A Method Based on Time Averaging Over Short, Modified Periodograms, *IEEE Trans. Audio Electroacoustics*, *AU-15*, 70–73.
- Winterwerp, J. C., and W. G. M. van Kesteren (2004), *Introduction to the Physics of Cohesive Sediments in the Marine Environment*, Dev. Sedimentol., vol. 56, Elsevier, New York.
- Winterwerp, J. C., W. G. M. van Kesteren, B. van Prooijen, and W. Jacobs (2012), A conceptual framework for shear flow-induced erosion of soft cohesive sediment beds, *J. Geophys. Res.*, *117*, C10020, doi:10.1029/2012JC008072.